

# Binder Effects on Processing, Mechanical Properties, and Performance of Thin Sulfide Solid-State Electrolytes

Yuanshun Li, Chanho Kim, Wenda Wu, Andre Adam, Fuead Hasan, Thomas Zawodzinski, Jagjit Nanda, and Guang Yang\*

All-solid-state batteries (ASSBs) offer enhanced safety and energy density compared to conventional lithium-ion batteries by replacing flammable liquid electrolytes with solid-state electrolytes (SSEs). Among SSEs, sulfide-based electrolytes exhibit high ionic conductivity and mechanical deformability, making them promising candidates for next-generation energy storage. However, their practical implementation is hindered by interfacial instability, mechanical brittleness, and challenges in fabricating ultrathin electrolyte membranes ( $<30\text{ }\mu\text{m}$ ) with robust mechanical integrity. This study systematically examines the influence of polymeric binders—polyisobutylene, hydrogenated nitrile butadiene rubber, and styrene–ethylene–butylene–styrene (SEBS)—on the structural, mechanical, and electrochemical performance of thin

sulfide SSE membranes. Key findings reveal that SEBS enables the fabrication of ultrathin, uniform membranes, while binder elasticity significantly affects structural stability during cycling. Operando stack pressure measurements indicate that binder properties directly influence adhesion force for LPSCl particles, influencing their stabilizing cycling period. These results underscore the critical role of polymer binders beyond mechanical reinforcement, positioning them as essential design variables in sulfide SSE engineering. By linking binder chemistry to processability and electrochemical performance, this study provides insights into optimizing sulfide SSEs, advancing their commercial viability in ASSBs.

## 1. Introduction

The increasing demand for high-energy-density and safer energy storage solutions has intensified research into ASSBs. Unlike conventional lithium-ion batteries (LIBs), which rely on flammable liquid electrolytes, ASSBs employ solid electrolytes, eliminating risks associated with leakage, thermal runaway, and dendrite-induced short circuits, significantly improving their safety profile.<sup>[1,2]</sup> Furthermore, the use of solid-state electrolytes (SSEs) enables the integration of lithium metal anodes, offering a boosted theoretical capacity than conventional graphite anodes, thus allowing for significant increases in energy density.<sup>[3]</sup>

These advantages position ASSBs as transformative technology for electric vehicles, grid storage, and next-generation portable electronics.

Among various SSEs, sulfide-based electrolytes have emerged as particularly promising due to their exceptionally high room-temperature ionic conductivities,<sup>[4,5]</sup> with comparable ionic conductivity with liquid electrolyte exceeding  $10^{-2}\text{ S cm}^{-1}$ , and their ability to be processed into dense films without high-temperature sintering.<sup>[6]</sup> In contrast, oxide-based electrolytes require elevated temperatures for densification and exhibit brittle mechanical properties that hinder their compatibility with electrodes. Sulfide SSEs, such as  $\text{Li}_{10}\text{GeP}_2\text{S}_{12}$  and argyrodite-type ( $\text{Li}_6\text{PS}_5\text{Cl}$ ) compounds, possess favorable mechanical deformability that enables better interfacial contact with electrodes, reducing interfacial resistance and improving electrochemical performance.<sup>[7]</sup> Despite these advantages, the practical implementation of sulfide SSEs remains hindered by several challenges, including interfacial instability, mechanical brittleness, and fabrication limitations.<sup>[8]</sup> Minimizing the thickness of the sulfide solid electrolyte layer is essential to maximize energy density in ASSBs. Conventional sulfide SSE layers are often hundreds of micrometers thick, which possesses high internal resistance, low ion transport efficiency, and limited practical energy and power densities.<sup>[9,10]</sup> Thick electrolyte layers contribute to sluggish kinetics, higher polarization, and lower overall battery efficiency. Thus, fabricating ultrathin (e.g.,  $<30\text{ }\mu\text{m}$ ) sulfide SSE membranes with high mechanical robustness and high ionic conductivity is crucial for the realization of high-performance ASSBs.<sup>[11,12]</sup> However, achieving such thin membranes while maintaining mechanical integrity remains a significant challenge, requiring innovations in processing and material design.

Y. Li, C. Kim, W. Wu, A. Adam, F. Hasan, T. Zawodzinski, G. Yang

Chemical Sciences Division  
Oak Ridge National Laboratory  
Oak Ridge, Tennessee 37831, USA  
E-mail: yangg@ornl.gov

Y. Li, T. Zawodzinski  
Department of Chemical and Biomolecular Engineering  
University of Tennessee Knoxville  
Knoxville, TN 37996, USA

J. Nanda  
Applied Energy Division  
SLAC National Laboratory  
Menlo Park, CA 94025, USA

G. Yang  
The Bredesen Center for Interdisciplinary Research and Graduate Education  
University of Tennessee Knoxville  
Knoxville, TN 37996, USA

 Supporting information for this article is available on the WWW under <https://doi.org/10.1002/batt.202500192>

Polymeric binders play a critical role in the fabrication and performance of thin, flexible sulfide-based SSEs. They provide mechanical cohesion, influence electrolyte processability, and directly impact electrochemical properties such as interfacial stability and long-term cycling performance.<sup>[13]</sup> While conventional slurry-based processing of sulfide SSEs often utilizes polymer binders to enhance mechanical strength, these binders can also impede lithium-ion transport if not carefully selected.<sup>[8]</sup> For example, the molecular weight of the binder directly affects the mechanical strength and flexibility of the SSE film, influencing its electrochemical stability and performance.<sup>[14]</sup> Moreover, physiochemical properties of binders determines interfacial interactions between the SSE, electrodes, and lithium metal anodes, making binder selection a crucial role for designing sulfide SSEs.<sup>[11]</sup>

To date, several research efforts have been dedicated to understanding and optimizing polymer binders for sulfide SSEs. For example, Riphaus et al. investigated the use various off-the-shelf rubbery polymers as binder materials for  $\text{Li}_{10}\text{SnP}_2\text{S}_{12}$  SSEs, finding that high polar binders improved mechanical stability but introduced high interfacial resistance.<sup>[11]</sup> Zhao et al. developed a novel polymeric binder based on dimethyl aminoethyl methacrylate and polyethylene glycol diacrylate, which demonstrated excellent adhesion and stability in  $\text{Li}_6\text{PS}_5\text{Cl}$  membranes while maintaining high ionic conductivity.<sup>[7]</sup> Su et al. explored a phase-transition approach using polycaprolactone as a binder, enabling the formation of compact electrolyte membranes that exhibited improved interfacial stability and ionic transport.<sup>[15]</sup> In a recent study from our team, we elucidated the effect of polymer binder molecular weight on SSE film performance, showing that higher molecular weight polymers enhanced film strength but also increased grain boundary resistance, leading to trade-offs in ionic transport.<sup>[16]</sup>

Recent studies have highlighted the advantages of rubbery polymer binders such as hydrogenated nitrile butadiene rubber (HNBR) and styrene–ethylene–butylene–styrene (SEBS), which exhibit superior elasticity and improve the mechanical stability of sulfide SSE membranes under repeated cycling.<sup>[17]</sup> These elastomeric materials enhance interfacial contact between electrolyte particles, reduce grain boundary resistance, and facilitate efficient lithium-ion transport. However, despite these promising results, the direct correlation between the chemical effects of binder on mechanical properties of ceramic film and the cycling performance of sulfide SSEs remains insufficiently understood.

This study systematically investigates the interplay between binders' physiochemical properties—specifically polyisobutylene (PIB), HNBR, and SEBS—and the structural, mechanical, and electrochemical properties of thin, flexible sulfide SSE membranes. Three key findings emerge from this work: 1) SEBS enables the fabrication of ultrathin SSE membranes (<30  $\mu\text{m}$ ) with uniform morphology, exceeding the thickness limitations of PIB- and HNBR-based counterparts; 2) operando stack pressure measurements indicates HNBR-based membranes, possessing stronger adhesion force to entangle LPSCI particles due to nitrile bond polarity, require less extensive formation cycles to stabilize the volume expansion of the film;

3) long-term cycling performance, including capacity retention and overpotential growth, is intrinsically linked to binder-driven ionic conductivity and interfacial phenomena, with PIB-based cells demonstrating superior stability and electrochemical performance.

These findings challenge the traditional perception of polymer binders as passive processing aids, instead positioning them as critical design variables in sulfide SSE engineering. By bridging the knowledge gaps between binder chemistry, processability, and cell-level performance, this study provides actionable guidelines for the rational design of sulfide-based SSEs, accelerating their integration into commercial ASSB technologies.

## 2. Results and Discussions

LPSCI thin films were prepared using pre-synthesized LPSCI (NEI Corp.) as the active material, toluene as the solvent, and different polymeric binders, including PIB, SEBS, and HNBR, to form the casting slurry. These binders were selected to represent three main high-molecular-weight polymer classes: homopolymers (PIB), block copolymers (SEBS), and copolymers (HNBR). SEBS and HNBR, both hydrated derivatives of SBS and NBR, were chosen for their enhanced oxidative stability against LPSCI particles. Toluene was identified as one of few optimal solvents due to its minimal structural and morphological impact on LPSCI membrane formation, as previously reported.<sup>[18]</sup> This fundamentally explained by its low polarity with weak Van Der Waals force, which are insufficient to induce chemisorption.<sup>[19]</sup>

Figure 1a presents the as-calendared LPSCI films incorporating PIB (control), SEBS, and HNBR at loadings of 1, 2, and 5 wt%. Notably, at 5 wt%, HNBR led to LPSCI slurry agglomeration due to its high viscosity at a measured value of 12 534 mPa S in Table S1, Supporting Information. Compared with viscosity of stock binder solution (7.4 wt% HNBR in toluene) at 286 mPa S without LPSCI, this significant difference suggests potential interactions between HNBR and LPSCI that may contribute to the slurry instability. Additionally, films containing 2% PIB, 1% PIB, and 1% SEBS exhibited poor adhesion, as evidenced by crack propagation observed during handling. To evaluate film elasticity, a Mandrel test was conducted (Figure 1b), with results summarized in Figure 1c. Among all formulations, HNBR-based films demonstrated the highest elasticity, with 2% HNBR maintaining structural integrity down to a 2 mm bending diameter, while even 1% HNBR sustained bending at 6 mm. Note that complementary tensile tests and nano-indentation experiments are preferred to quantify the mechanical stress in improving the reliability and reproducibility.<sup>[20]</sup> Since rubber-based polymers do not contribute to the ionic or electronic conductivity, optimizing LPSCI membranes requires minimizing binder content while maintaining mechanical integrity to achieve scalable, thinner films for improved performance.

To evaluate the ionic conductivity of the films, EIS was conducted using stainless steel blocking electrodes to measure the

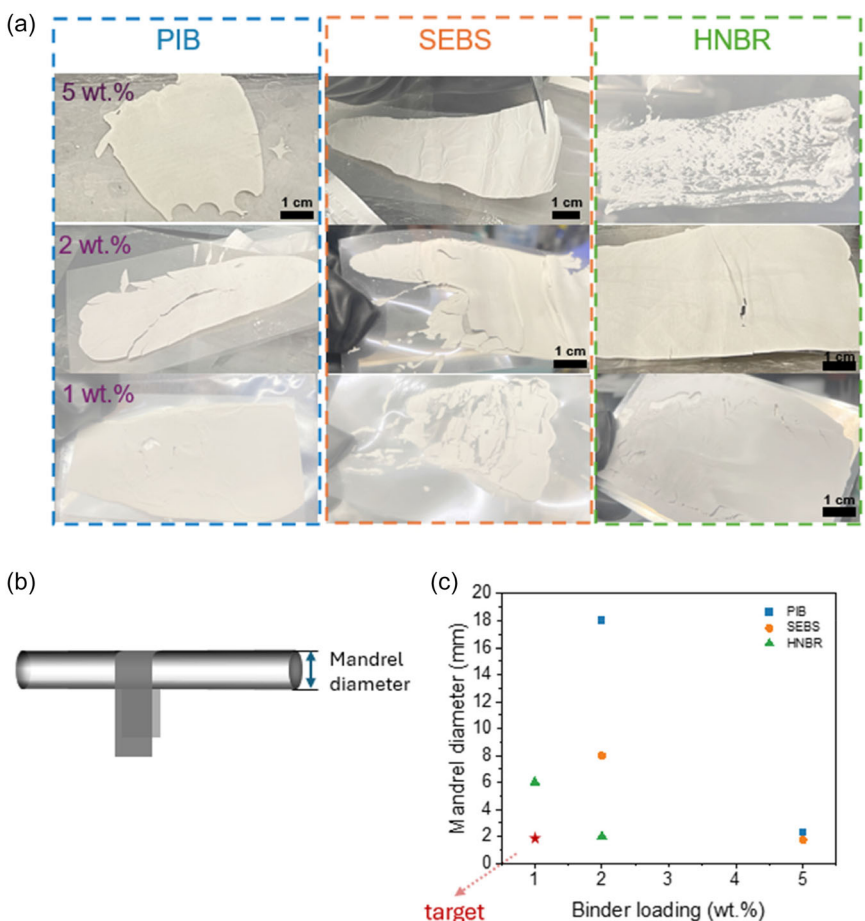


**Figure 1.** a) Pristine LPSCl films with different binders (PIB, SEBS, and HNBR) at loadings of 1, 2, and 5 wt%, demonstrating the critical role of binders in fabricating free-standing films. b) Mandrel bending tests conducted using a 3D-printed bar with diameters ranging from 2 mm to 20 mm to evaluate film flexibility. c) Summary of mandrel test results in a plot of mandrel diameter versus binder loading, highlighting the goal of achieving high elasticity (<2 mm bending diameter) while maintaining high ionic conductivity (<1 wt% binder loading).

impedance of LPSCl films and accurately determine the bulk electrolyte resistance. Figure 2a presents the Nyquist plots for the 5% PIB film across a temperature range from 80 °C to 30 °C, while Nyquist plots for other films are included in Figure S2, Supporting Information. A high-frequency semicircle progressively emerges as the temperature decreases, suggesting that grain boundary resistance becomes the dominant factor at lower temperatures, consistent with previous reports.<sup>[21,22]</sup>

Figure 2b compares the ionic conductivity of different binder-containing films as a function of temperature. At high temperatures (>60 °C), where grain boundary effects are minimal, the 2% SEBS film exhibits the highest conductivity, outperforming both the 5% PIB and 2% HNBR films. However, as the temperature decreases, the 5% PIB film demonstrates superior conductivity, reaching 0.8 mS/cm at 30 °C, where grain boundary resistance dominates. This suggests that PIB may help reduce space charge potential at LPSCl particle interfaces.<sup>[23]</sup> Figure 2c presents cross-sectional scanning electron microscopy (SEM) images of the 5% PIB, 2% SEBS, and 2% HNBR films, while Figure 2d compares film thickness, analyzed using an in-house algorithm (detailed in Figure S3, Supporting Information). Notably, the 2% SEBS film exhibits a significantly reduced

thickness ( $\approx 27 \mu\text{m}$ ), nearly three times thinner than the other films, which can be attributed to the lower viscosity of the SEBS slurry. Figure 2e presents the porosity results of each film using a threshold-tuning from 36 to 39 based on ImageJ. This allows us to better cover possible porosity boundary error range within 5% difference in Figure S3c, Supporting Information, revealing that the PIB binder results in the lowest porosity with a more efficient ionic pathway.

To investigate the chemical and structural changes in pristine LPSCl films induced by binders and toluene during wet processing, Fourier-transform infrared spectroscopy (FTIR) and Raman spectroscopy were conducted (Figure 3a–c). FTIR analysis (Figure 3a) shows that  $\nu(\text{P}-\text{O})$  in  $\text{PO}_4^{3-}$  ( $\approx 1100 \text{ cm}^{-1}$ ) and  $\nu(\text{O}-\text{H})$  ( $\approx 3000-3500 \text{ cm}^{-1}$ ) are barely detectable in binder-loaded LPSCl films, indicating minimal hydrolysis reaction during processing.<sup>[24]</sup> Figure 3b examines the local structural changes of  $\nu(\text{P}-\text{S})$  under different processing conditions. The highest P–S bond frequency is observed in the 5% PIB film compared to the 2% SEBS and 2% HNBR films, suggesting a better stability of the  $\text{PS}_4^{3-}$  framework in the 5% PIB sample, which correlates with its highest ionic conductivity. Raman spectra further support this observation, with a P–S stretching peak near

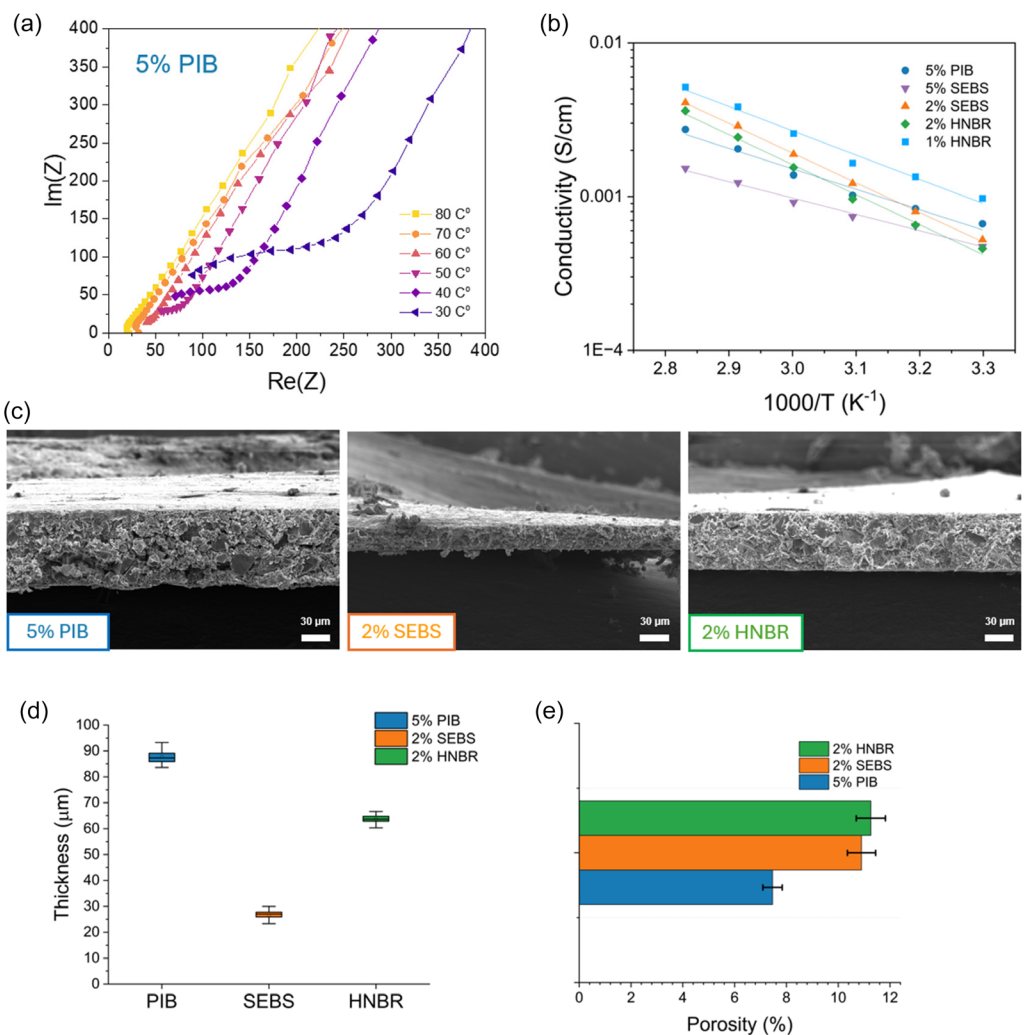
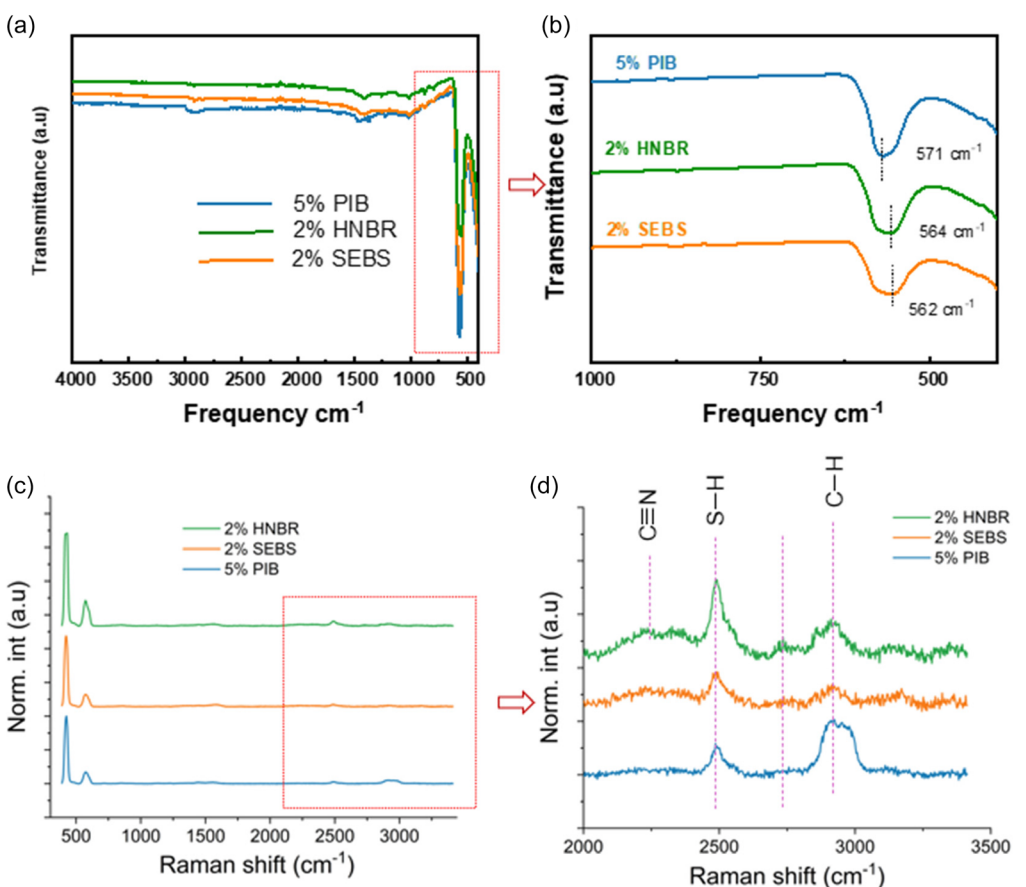


**Figure 2.** a) Temperature-dependent Nyquist plots of as-prepared 5% PIB LPSCl films measured from 30 °C to 80 °C. b) Conductivity as a function of temperature for five different films: 5% PIB, 5% SEBS, 2% SEBS, 2% HNBR, and 1% HNBR. c) Cross-sectional SEM images of 5% PIB, 2% SEBS, and 2% HNBR films. Computational image analysis of d) film thickness and e) porosity, where the error bar for thickness is derived from pixel-based measurements in 30 μm resolution images (Figure S2d, Supporting Information), and the error bar for porosity reflects variations from threshold tuning (Figure S2c, Supporting Information).

425 cm<sup>-1</sup> (provided in Figure S4, Supporting Information). Interestingly, all processed films exhibit a newly emerged peak at  $\approx 2500 \text{ cm}^{-1}$  (Figure 3d), attributed to S—H bond formation due to interactions between toluene and LPSCl. Additionally, a peak at 2734.5 cm<sup>-1</sup> is detected exclusively in the 2% HNBR film, which likely indicates that an interaction between nitrile group and LPSCl. Further FTIR analysis of pristine HNBR (Figure S5, Supporting Information) reveals a characteristic C=O bond near 1726 cm<sup>-1</sup>, attributed to manufacturing defects from ester end-functionalization during HNBR synthesis.<sup>[25]</sup> This structural vulnerability greatly compromises the stability of HNBR film during wet processing.

We evaluated the processability and galvanostatic cycling performance of sulfide SSBs using LPSCl films with different binders and loadings. To ensure intimate contact between electrodes and solid electrolytes, high stacking pressure is typically applied in all-solid-state cell fabrication. However, excessive pressure ( $>25 \text{ MPa}$ ) can lead to Li metal infiltration into the

electrolyte, causing immediate short circuit.<sup>[26]</sup> To mitigate this issue, indium metal was used as the anode, as it can tolerate high stacking pressure and exhibits significantly lower volumetric expansion compared to Si-based anodes. This setup effectively allows the full cell performance evaluation of LPSCl thin films with different binders. **Figure 4a** presents the long-term cycling stability of various LPSCl films at 0.2 mA cm<sup>-2</sup>. The 5% PIB-based film demonstrates superior initial capacity, averaging 125 mAh g<sup>-1</sup>, with a capacity retention of 79.7% after consecutive 200 charge-discharge cycles. In contrast, the 2% SEBS and 2% HNBR films exhibit moderate capacity degradation. 5% SEBS and 1% HNBR all come with practical fabrication challenges. Specifically, high elasticity film (5% SEBS) tends to bend over, while 1% HNBR is prone to form microstructure cracks. Based on these results, the remainder of this study will focus on 5% PIB, 2% SEBS, and 2% HNBR to enable a fair comparison of the electrochemical and mechanical performance of LPSCl films.



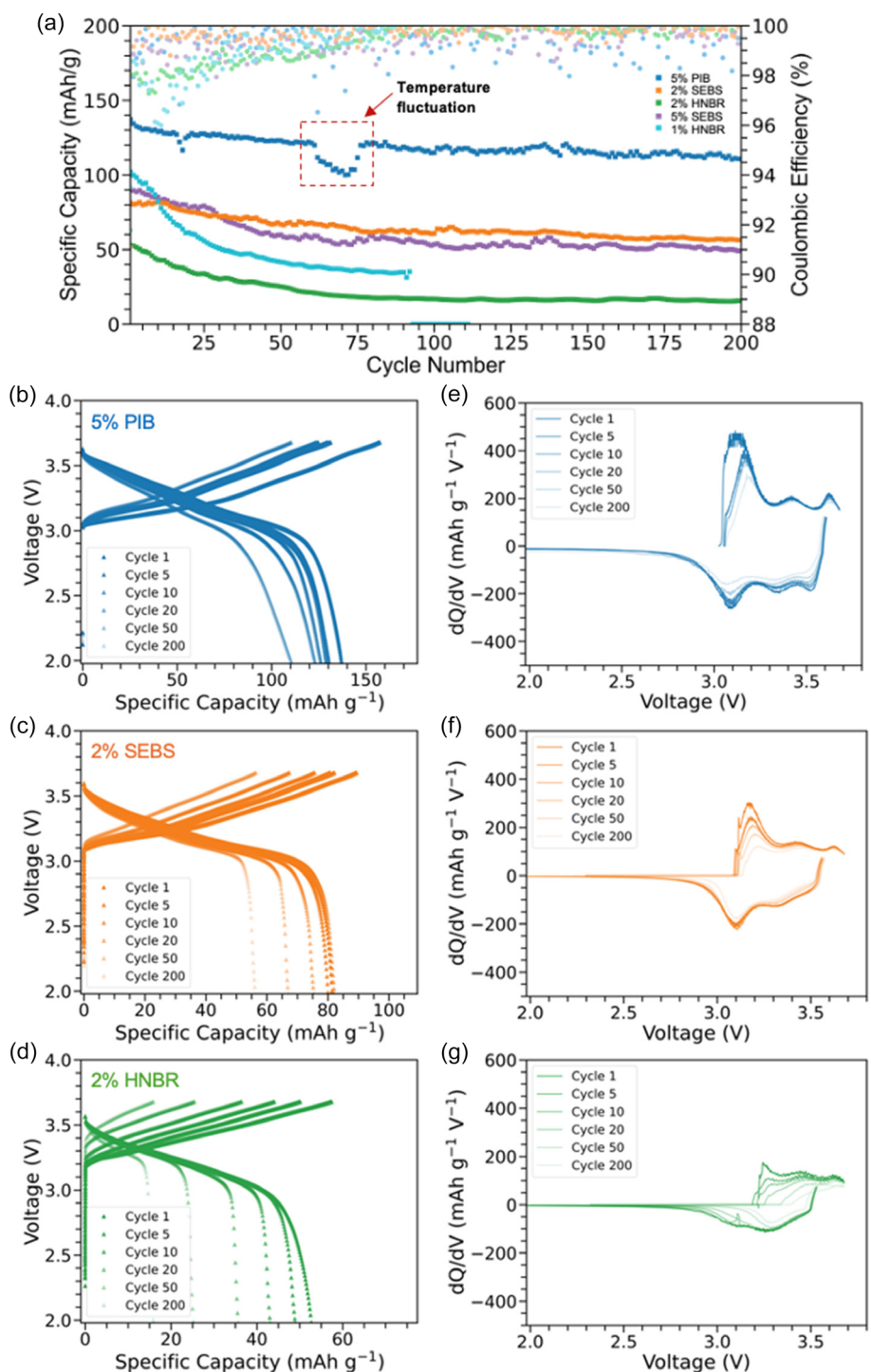
**Figure 3.** a) FT-IR spectra of as-calendared LPSCl films with 5% PIB, 2% HNBR, and 2% SEBS. b) Zoomed-in FT-IR spectra highlighting the wavelength shift in the P-S peak around 570 cm<sup>-1</sup>, indicating binder-induced processing effects. c) Raman spectra of LPSCl films with different polymer binders, with subtle spectral differences. d) Zoomed-in Raman spectra emphasizing organic-related peaks.

Figure 4b–d present the voltage–capacity profiles from the 1st to the 200th cycle for 5% PIB, 2% SEBS, and 2% HNBR films. Compared to 5% PIB, the 2% SEBS film exhibits moderate degradation, with a capacity fade of 0.15% per cycle, while the 2% HNBR film undergoes more severe degradation, losing 0.35% capacity per cycle. Neither 2% SEBS nor 2% HNBR achieves a deliverable capacity comparable to that of 5% PIB, consistent with the higher ionic conductivity observed in the 5% PIB film. To further analyze electrochemical kinetics, differential capacity ( $dQ/dV$ ) vs. voltage analysis was conducted (Figure 4e–h). The 5% PIB and 2% SEBS films exhibit similar kinetic behavior, as indicated by a dominant peak near  $\approx$ 3.16 V, which corresponds to the NMC phase transition (M-H1),<sup>[27]</sup> though further deconvolution from Li<sub>x</sub>In alloy phase is required for precise attribution. In contrast, the 2% HNBR film displays sluggish kinetics, evidenced by a peak shift to 3.25 V during the first-cycle lithiation. This 0.09 V increase in overpotential is likely due to local structural defects in the 2% HNBR film and an unstable electrode–electrolyte interphase, contributing to increased resistance and performance degradation.

To identify the dominant limiting factors in electrochemical processes during cycling, *in situ* EIS was performed throughout the first charge–discharge cycle. The impedance data were analyzed using distribution of relaxation time (DRT), which

enables unsupervised determination of the equivalent circuit, enhancing accuracy by capturing the full range of electrochemical processes without prior assumptions. Recent systematic and validated DRT studies in the field of ASSBs have demonstrated its reliability and are continuously expanding its applicability.<sup>[28,29]</sup> Unlike traditional LIB, ASSBs exhibit significantly more complex electrochemical behavior, including pronounced grain boundary resistance in solid electrolytes and multiple interfacial resistances. Given these complexities, DRT is a crucial tool for providing a detailed and nuanced understanding of electrochemical processes in solid-state batteries.

Figure 5a–c present time-resolved DRT analysis during the first charging cycle from 3.2 V to 3.678 V (full lithiation) over a time range of  $10^{-6}$  to  $10^{-2}$  s (the full range frequency DRT plots has been included in Figure S6, Supporting Information). The thermal voltage bar represents the corresponding SOC. The 5% PIB film exhibits a progressive increase in bulk impedance at  $10^{-6}$  s upon lithiation, suggesting volume expansion of the LPSCl thin film. In contrast, both the 2% SEBS and 2% HNBR films show minimal bulk impedance changes, indicating that the 5% PIB film is more sensitive to structural changes during the formation cycle. Notably, the 2% HNBR film exhibits more than twice the bulk impedance of the 5% PIB and 2% SEBS films, consistent



**Figure 4.** a) Galvanostatic cycling performance of LPSCl thin films with different polymer binders and loadings: 5% PIB (control), 2% SEBS, 2% HNBR, 5% SEBS, and 1% HNBR. Voltage vs. specific capacity plots at cycles 1, 5, 10, 20, 50, and 200 for b) 5% PIB, c) 2% SEBS, and d) 2% HNBR. Corresponding  $dQ/dV$  analysis for e) 5% PIB, f) 2% SEBS, and g) 2% HNBR, illustrating kinetic responses during the charge-discharge process.

with its lower ionic conductivity, as previously observed in Figure 2b. Additionally, an unexpected peak at  $10^{-5}$  s appears exclusively in the 2% HNBR film, which is attributed to grain boundary impedance. This suggests that the functional group effects of HNBR negatively impact LPSCl film performance in the cell. Furthermore, the absence of significant differences between charging and discharging processes (Figure 5d-f)

reinforces the reliability of the DRT analysis in capturing electrochemical behavior.

The speculating volume expansion is perfectly justified in the mechano-force displacement experiment. Figure 5g illustrates the house-customized operando pressure monitor setup dedicated to solid-state cells. Upon charging, indium lithiation creates a volume expansion which is much more severe than

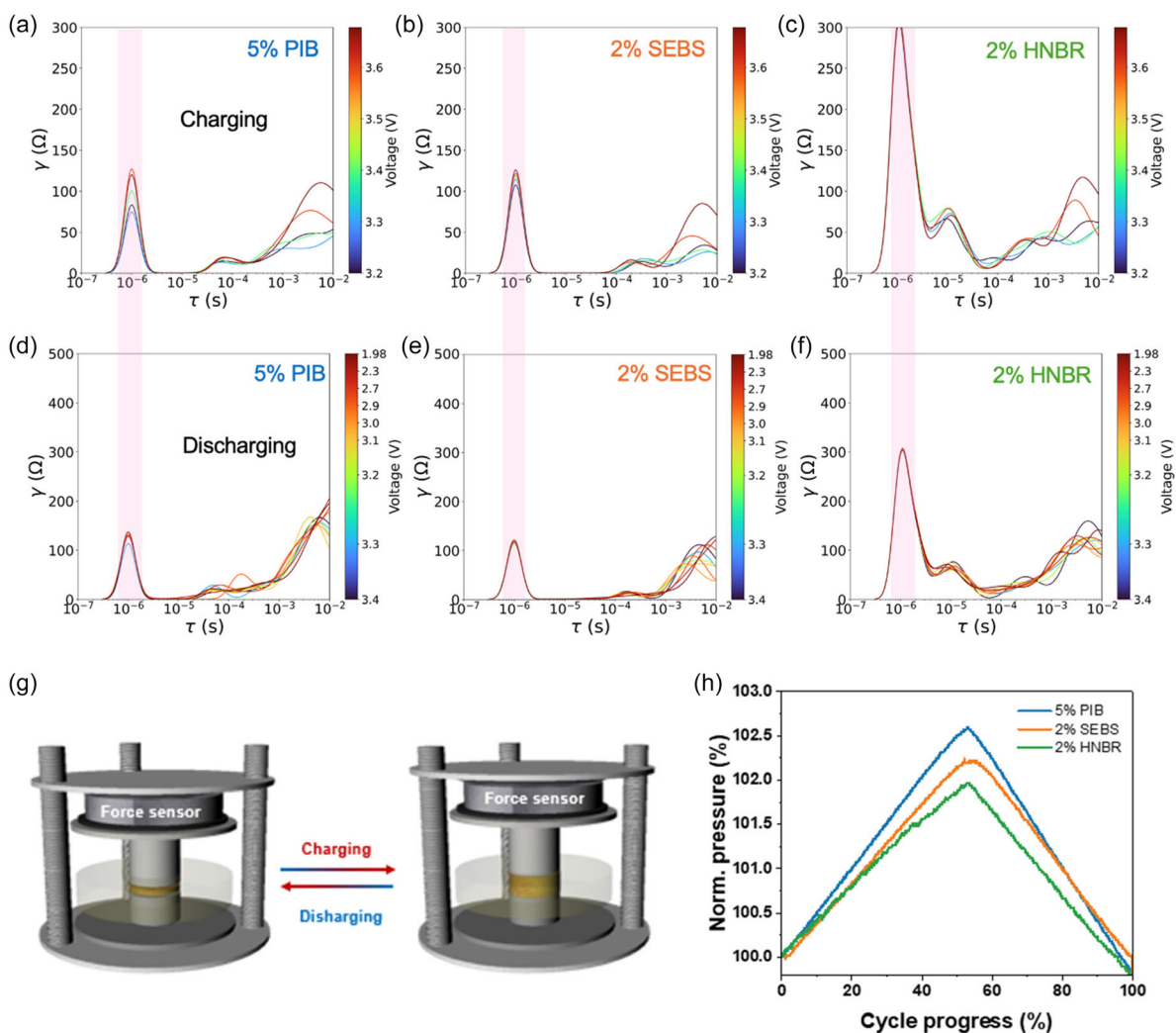


**Figure 5.** DRT analysis for SOC dependent EIS data in initial a–c) charging step and d–f) discharging step, highlighting the relaxation time range from  $10^{-7}$  to  $10^{-2}$  s ( $10^6$  to 100 Hz). g) A demonstration of force displacement experiment mechanism. h) Displacement force curve for operando monitoring pressure change during lithiation and delithiation in first cycle (after formation cycle) among all binder LPSCI films cells with pressure normalized to its initial state before lithiation at 420 kg.

cathode shrinkage. The binder plays an important role in providing strong adhesion between LPSCI particles to adapt volume expansion stress and minimize the LPSCI separator volume change during these processes. This ensures the interfacial contacts in both cathode and anode-electrolyte interphases. Figure 5h presents different binder films force displacement response in one cycle. All films behave expectably expansion during charging and shrinkage during discharging. The 5% PIB film presents 2.6% pressure gauge during lithiation, which is 0.3% higher than 2% SEBS, and 0.7% larger than 2% HNBR. This indicates the PIB binder has the lowest adhesion force to stabilize LPSCI particle.

Raman mapping was performed on the cross-sectional area of the cell to localize LPSCI thin films and the cathode. The spectral data were analyzed using unsupervised machine learning via K-means clustering, enabling the detection of subtle structural changes. Figure 6a presents five clusters corresponding to different chemical compositions, allowing identification of structural modifications during cycling. In both the 5% PIB (Figure 6a)

and 2% SEBS (Figure 6d) films, all clusters exhibit a single peak at  $425\text{ cm}^{-1}$ , indicating an intact P–S stretching bond. In contrast, the 2% HNBR film shows an additional minor peak at  $375\text{ cm}^{-1}$ , attributed to the  $\text{PS}_3$  (phosphorus trisulfide) stretching mode.<sup>[30]</sup> This suggests that the 2% HNBR favored a reduction pathway that forms undesired  $\text{PS}_3$  product, which disrupted the LPSCI structure. The cathode electrolyte interphase exhibits more heterogeneous structural features in the 5% PIB film compared to the 2% SEBS film, as visualized in the Raman mapping images (Figure 6b,e) and further quantified in Figure 6c,f. This aligns with prior observations that the 5% PIB cell achieves better NMC utilization and higher deliverable capacity. Interestingly, Figure 6h reveals a poorly defined interphase in the 2% HNBR cell, characterized by dispersed green clusters appearing in both the LPSCI thin film and the cathode. This feature likely originates from the deformed 2% HNBR film, which exhibits moderate grain boundary resistance. Thus, Raman mapping further validates and confirms the detrimental impact of 2% HNBR defects on chemical and structural degradation after cycling.

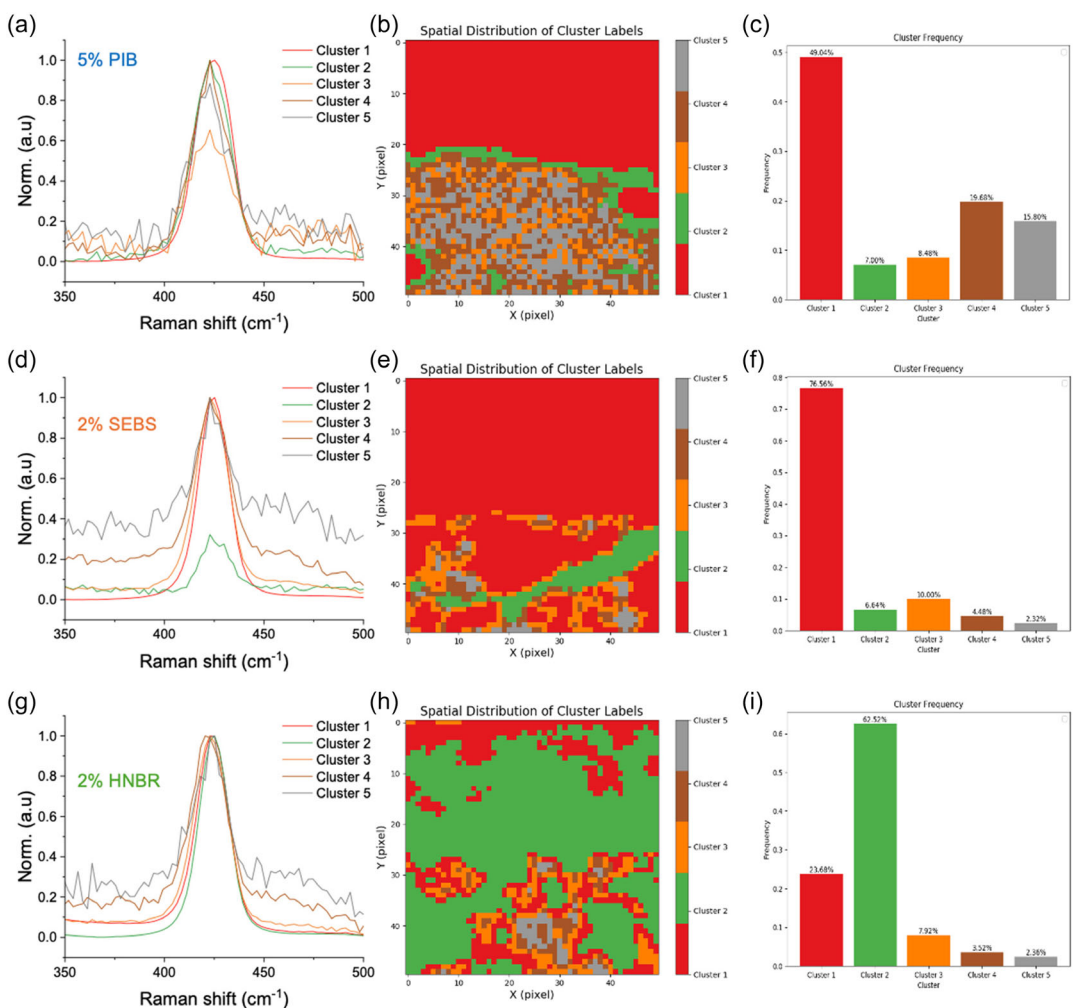


**Figure 6.** Multivariable analysis results of Raman mapping by K-means clustering method for a) 5% PIB, d) 2% SEBS, and g) 2% HNBR. Their corresponding cluster spatial distribution in panels b) 5% PIB, e) 2% SEBS, and h) 2% HNBR, highlighting the dominating chemical structural change by visualizing the analytical structural distribution for cathode-LPSCI film interphase. Panels of c) 5% PIB, f) 2% SEBS, and i) 2% HNBR present the statistic percentage of different clusters, reporting the quantified Raman cluster mapping analysis across the image.

### 3. Conclusion

This study systematically investigated the effects of rubbery binders on the correlation between mechanical properties and electrochemical performance of LPSCI SSEs. We found that SEBS enables the fabrication of an ultrathin (30 µm) free-standing LPSCI film while maintaining cyclable cell performance. However, PIB remains the optimal choice for cycling capacity and stability, primarily due to its superior room-temperature ionic conductivity. In contrast, HNBR was found to be incompatible with LPSCI processing in toluene, as evidenced by its high grain boundary resistance in DRT analysis and the flooding phenomena observed in Raman mapping. Additionally, we performed force-displacement experiments for the first time to evaluate the binder effects on sulfide SSEs, revealing differences in volume expansion during lithiation and delithiation. Our findings emphasize that binders play an important role in SSEs that not only affects the mechanical strength of as-prepared films but also greatly impacts the conductivity and stability of electrolytes and in situ formed electrode interphases. Focusing on

developing new PIB or SEBS-based polymer with a well balance between ionic conductivity and film thickens is a potentially valuable direction for enhancing the electrochemical performance of ASSBs.

### 4. Experimental Section

#### LPSCI Thin Film Fabrication

PIB ( $M_w \approx 1270 \text{ kg mol}^{-1}$  from Scientific Polymer Products, Inc., New York, US), SEBS (MTI Corp.), and HNBR (LT1707) were dried at 80 °C under vacuum overnight and dissolved in anhydrous toluene with 4 Å molecular sieves, respectively. Stock solutions were prepared at 7.4 wt% rubber binder and used for electrolyte slurry preparations. The solid electrolyte thin films were fabricated following previous methods, where rubber binder and Li<sub>6</sub>PS<sub>5</sub>Cl argyrodite (3–5 µm; NEI Corp., New Jersey, US) were milled in different weight ratio including 5:95, 2:98, and 1:99. A 50:50 solvent-to-solid weight ratio was maintained in the slurry, which was ball-milled overnight ( $\geq 18$  h) with zirconia milling media under low-velocity mixing before being returned to an Ar-filled glovebox. The viscosity of stock solutions and LPSCI slurry was measured by glovebox-enclosed

rheometer with 30 rpm in Figure S1, Supporting Information. The slurry was doctor-bladed onto a nonstick mylar sheet, dried at room temperature, and sealed in a pouch between mylar sheets for calendaring outside the glovebox. Cold pressing (MTI cold roller press, MSK-HRP-MR100DC) was performed at room temperature with progressively thicker shims to reduce the thickness of the electrolyte. The densified films were promptly returned to the glovebox and dried under vacuum overnight before use.

### Composite Cathode Synthesis

The composite cathode was prepared by TURBULA mixer for 1 h, in a ratio of 60:35:5 of LiNbO<sub>3</sub>-NMC811 active material, LPSCl solid electrolyte, and vapor-grown carbon fibers. The ratio of cathode materials and balling media is controlled as 1:10.

### Electrochemical Evaluations

Electrochemical evaluations were performed in 6 mm-diameter PEEK cells (Solid Solutions, 7815-C6) at room temperature within an argon-filled glovebox, following the established protocol of our research group. Two 6 mm films of rubber binder-LPSCl were centrally positioned in the mold and secured by applying 20 bars of pressure for 10 s, after which a 6 mm slurry-cast cathode was inserted and cold-pressed for 3 min at 60 bars. A 5 mm-diameter indium foil (150 × 150 TF, Custom Thermoelectric) and a 6 mm-diameter copper foil were then placed as the anode, and the assembled cell underwent electrochemical testing, including galvanostatic cycling, and state of charge (SOC)-dependent electrochemical impedance spectroscopy (EIS). Galvanostatic cycling involved three formation cycles at 0.02 C, followed by standard cycling at 0.1 C between 1.98 and 3.678 V vs. Li<sub>x</sub>In for 200 cycles under a stack pressure of ≈30 MPa. SOC-dependent EIS was performed by charging or discharging at 0.1 C to the target potential, followed by a 30 min rest to reach a steady state before impedance measurement from 1 MHz to 50 mHz. DRT analysis was carried by pyDRTtools developed in Ciucci's lab with discretization method and second regularization fitting.<sup>[31,32]</sup>

To test the ionic conductivity of the film, three 6 mm-diameter disc films of rubber binder-LPSCl were positioned in the same PEEK mold and secured by applying 40 bars of pressure for 3 mins. Temperature dependent EIS measurement was executed from 80 to 30 °C in 10 °C increments for 3 cycles using Biologic VMP3 with frequency scan range between 1 and 100 MHz with an excitation amplitude of 10 mV.

### SEM

Microstructural analysis was conducted using a Zeiss Merlin FE-SEM at an acceleration voltage of 15 kV to examine the microstructure of samples. The imaging was performed using secondary electron detection, allowing for detailed visualization of thickness and porosity. The SEM images were processed using ImageJ.<sup>[33]</sup> A mask was applied to each SEM image to isolate the film cross section. The cross section was then binarized using the isodata algorithm, and the threshold was further adjusted to best match the most prominent pores and particles observed in the raw SEM. An in-house algorithm was developed to procedurally measure the thickness of each column of pixels, thus computing the thickness spatial distribution along the length of the cross-section from each SEM.

### FTIR

All Infrared spectra were collected by a Bruker ALPHA II compact FT-IR spectrometer.

### Raman Mapping

Raman mapping was conducted using a Horiba XploRA confocal Raman system equipped with a 405 nm UV laser. To prevent potential sample damage, the laser power was carefully maintained below 500 μW. The measurements were performed at 50× magnification, achieving a spatial resolution with a spot size of ≈1 μm. A diffraction grating with 1800 grooves per millimeter was employed for spectral acquisition. The mapping process covered a 50 × 50 grid, resulting in the collection of spectra from 2500 distinct points. Each pixel corresponded to a 1 × 1 μm<sup>2</sup> area, and spectral similarities were analyzed to classify regions with common peak characteristics into distinct clusters. The data were processed and analyzed using Horiba LabSpec 6 imaging and spectroscopy software, which enabled precise spectroscopic evaluation and clustering of spectral features.<sup>[34,35]</sup>

### Acknowledgements

This research was conducted at the Oak Ridge National Laboratory, managed by UT-Battelle, LLC, for the U.S. Department of Energy (DOE) and is sponsored by the Office of Energy Efficiency and Renewable Energy (EERE) in the Vehicle Technologies Office (VTO) through the Advanced Battery Materials Research (BMR) Program, managed by Drs. Simon Thompson and Tien Duong. This manuscript has been authored by UT-Battelle, LLC, under Contract No. DE-AC05-00OR22725 with the U.S. Department of Energy. SEM research was conducted as part of a user project at the Center for Nanophase Materials Sciences (CNMS), which is a US Department of Energy, Office of Science User Facility at Oak Ridge National Laboratory.

### Conflict of Interest

The authors declare no conflict of interest.

### Data Availability Statement

The data that support the findings of this study are available from the corresponding author upon reasonable request.

**Keywords:** argyrodite sulfide electrolyte • electrolyte performance • polymer binder • solid-state batteries • thin sheet membranes

- [1] J. Janek, W. G. Zeier, *Nat. Energy* **2016**, *1*, 16141.
- [2] N. Kamaya, K. Homma, Y. Yamakawa, M. Hirayama, R. Kanno, M. Yonemura, T. Kamiyama, Y. Kato, S. Hama, K. Kawamoto, A. Mitsui, *Nat. Mater.* **2011**, *10*, 682.
- [3] Y. Kato, S. Hori, T. Saito, K. Suzuki, M. Hirayama, A. Mitsui, M. Yonemura, H. Iba, R. Kanno, *Nat. energy* **2016**, *1*, 1.
- [4] J. Zhang, X. Xiao, J. Chen, H. Wan, N. Zhang, G. Liu, X. Yao, *Mater. Sci. Eng.: R: Rep.* **2025**, *164*, 100972.
- [5] G. Liu, J. Zhang, J. Yang, J. Chen, X. Xiao, X. Yao, *J. Energy Chem.* **2025**, *100*, 50.
- [6] A. Sakuda, A. Hayashi, M. Tatsumisago, *Sci. Rep.* **2013**, *3*, 2261.
- [7] X. Zhao, L. Shen, N. Zhang, J. Yang, G. Liu, J. Wu, X. Yao, *Energy Mater. Adv.* **2024**, *5*, 0074.
- [8] A. Mills, G. Yang, W.-Y. Tsai, X. C. Chen, R. L. Sacci, B. L. Armstrong, J. D. T. Hallinan, J. Nanda, *J. Electrochem. Soc.* **2023**, *170*, 080513.

- [9] Y. Li, C. Kim, E. Williams, Y. Su, J. Nanda, G. Yang, *Energy Environ. Mater.* **2025**, *8*, e12858.
- [10] N. Zhang, Q. He, L. Zhang, J. Zhang, L. Huang, X. Yao, *Adv. Mater.* **2024**, *36*, 2408903.
- [11] N. Riphaus, P. Strobl, B. Stiaszny, T. Zinkevich, M. Yavuz, J. Schnell, S. Indris, H. A. Gasteiger, S. J. Sedlmaier, *J. Electrochem. Soc.* **2018**, *165*, A3993.
- [12] N. Zhang, X. Zhao, G. Liu, Z. Peng, J. Wu, M. Men, X. Yao, *eTransportation* **2024**, *20*, 100319.
- [13] R. Li, N. Chen, S. Liu, Y. Mao, Z. Liao, K. Qiu, P. Wang, T. Zhang, S. Hao, G. Zhu, *Adv. Funct. Mater.* **2024**, *34*, 2409403.
- [14] A. Mills, S. Kalnaus, W.-Y. Tsai, Y.-F. Su, E. Williams, X. Zheng, S. Vaidyanathan, D. Hallinan Jr, T.J. Nanda, G. Yang, *ACS Energy Lett.* **2024**, *9*, 2677.
- [15] Z. Su, Q. Zhou, J. Jin, S. Yang, G. Li, J. Zhang, *Adv. Sci.* **2024**, *11*, 2407798.
- [16] A. Mills, S. Kalnaus, W.-Y. Tsai, Y.-F. Su, E. Williams, X. Zheng, S. Vaidyanathan, D. T. J. HallinanNanda Jr, Nanda, J., G. Yang, *ACS Energy Lett.* **2024**, *9*, 2677.
- [17] J. H. Teo, F. Strauss, Đ. Tripković, S. Schweidler, Y. Ma, M. Bianchini, J. Janek, T. Brezesinski, *Cell Rep. Phys. Sci.* **2021**, *2*, 100465.
- [18] A. Mills, W.-Y. Tsai, T. Brahmhatt, E. C. Self, B. L. Armstrong, D. T. Hallinan, J. Nanda, G. Yang, *MRS Commun.* **2023**, *13*, 1063.
- [19] X. Zhao, P. Xiang, J. Wu, Z. Liu, L. Shen, G. Liu, Z. Tian, L. Chen, X. Yao, *Nano Lett.* **2023**, *23*, 227.
- [20] H. Zhu, Z. Jia, Y. Chen, N. Weadock, J. Wan, O. Vaaland, X. Han, T. Li, L. Hu, *Nano Lett.* **2013**, *13*, 3093.
- [21] P. Bron, S. Dehnen, B. Roling, *J. Power Sources* **2016**, *329*, 530.
- [22] Y. Li, M. Lehmann, L. Cheng, T. A. Zawodzinski, J. Nanda, G. Yang, *Mater. Adv.* **2024**, *5*, 9138.
- [23] T. Ogunfunmi, X. Peng, H. Chu, J. Watt, J. Rupp, M. C. Scott, *Microsc. Microanal.* **2024**, *30*, 1781.
- [24] Y.-T. Chen, M. A. T. Marple, D. H. S. Tan, S.-Y. Ham, B. Sayahpour, W.-K. Li, H. Yang, J. B. Lee, H. J. Hah, E. A. Wu, J.-M. Doux, J. Jang, P. Ridley, A. Cronk, G. Deysher, Z. Chen, Y. S. Meng, *J. Mater. Chem. A* **2022**, *10*, 7155.
- [25] J. Liu, J. Sun, Z. Zhang, H. Yang, X. Nie, *ChemistryOpen* **2020**, *9*, 374.
- [26] J.-M. Doux, H. Nguyen, D. H. S. Tan, A. Banerjee, X. Wang, E. A. Wu, C. Jo, H. Yang, Y. S. Meng, *Adv. Energy Mater.* **2020**, *10*, 1903253.
- [27] K. J. Park, H. G. Jung, L. Y. Kuo, P. Kaghazchi, C. S. Yoon, Y. K. Sun, *Adv. Energy Mater.* **2018**, *8*, 1801202.
- [28] C.-Y. Yu, J. Choi, J. Dunham, R. Ghahremani, K. Liu, P. Lindemann, Z. Garver, D. Barchiesi, R. Farahati, J.-H. Kim, *J. Power Sources* **2024**, *597*, 234116.
- [29] Z. Tang, A. Morchhale, J. R. Sayre, J.-H. Kim, *J. Energy Storage* **2025**, *107*, 114966.
- [30] R. Rao, B. S. Conner, J. Jiang, R. Pachter, M. A. Susner, *J. Chem. Phys.* **2023**, *159*, 224706.
- [31] A. Maradesa, B. Py, T. H. Wan, M. B. Effat, F. Ciucci, *J. Electrochem. Soc.* **2023**, *170*, 030502.
- [32] T. H. Wan, M. Saccoccia, C. Chen, F. Ciucci, *Electrochim. Acta* **2015**, *184*, 483.
- [33] C. A. Schneider, W. S. Rasband, K. W. Eliceiri, *Nat. Methods* **2012**, *9*, 671.
- [34] G. Yang, R. Tao, C. J. Jafta, C. Shen, S. Zhao, L. He, I. Belharouak, J. Nanda, *J. Phys. Chem. C* **2021**, *125*, 13146.
- [35] G. Yang, X. Li, Y. Cheng, M. Wang, D. Ma, A. P. Sokolov, S. V. Kalinin, G. M. Veith, J. Nanda, *Nat. Commun.* **2021**, *12*, 578.

---

Manuscript received: March 16, 2025

Revised manuscript received: May 13, 2025

Version of record online:

---